Signatures of UV radiation around low-mass protostars in the Serpens Main with IRAM 30m

Agnieszka Mirocha[1,2], Agata Karska[2], Lars E. Kristensen[3], Marcin Gronowski[4], Miguel Figueira[5], Marcin Gładkowski[2,6], Michał Żółtowski[2], and Łukasz Tychoniec[7]

[1] Astronomical Observatory of the Jagiellonian University, ul. Orla 171, 30-244 Kraków, Poland
e-mail: `amirocha@doctoral.uj.edu.pl`
[2] Centre for Astronomy, Faculty of Physics, Astronomy and Informatics, Nicolaus Copernicus University, ul. Grudziądzka 5, 87-100 Toruń, Poland
[3] Centre for Star and Planet Formation, Niels Bohr Institute and Natural History Museum of Denmark, University of Copenhagen, Øster Voldgade 5-7, DK-1350 Copenhagen K, Denmark
[4] Institute of Physical Chemistry Polish Academy of Sciences, ul. Kasprzaka 44/52, 01-224 Warszawa, Poland
[5] National Centre for Nuclear Research, ul. Pasteura 7, 02-093 Warszawa, Poland
[6] Nicolaus Copernicus Astronomical Center, ul. Rabiańska 8, 87-100 Toruń, Poland
[7] Leiden Observatory, Leiden University, P.O. Box 9513, NL-2300RA Leiden, The Netherlands

ABSTRACT

Context. The Serpens Main is one of the most studied star forming region containing low-mass protostars. Observations at submillimetre range allow to determine physical and chemical processes around young stellar objects.
Aims. We aim to characterise the UV radiation in the surroundings of the low-mass protostars. We analyse the exitation and spatial extent of HCN, CN, CS and their isotopologues to identify the underlying processes. We can investigate the feedback from protostars and the excitation mechanisms of molecules.
Methods. We present $\sim$ 30 arcmin^2 IRAM 30m maps of CN $J = 1 - 0$, HCN $J = 1 - 0$, and CS $J = 3 - 2$ encompassing 10 Class 0/I protostars. We calculate HCN and CN column densities toward protostars and selected outflows positions. The column densities are compared with the Nahoon astrochemical model of molecules abundaces in order to characterise UV radiation field.
Results. Emission of HCN $J = 1 - 0$ and CS $J = 3 - 2$ is co-spatial with outflows, whereas CN emission peaks at the positions of protostars. CN and HCN column densities are of the order of 10^{13}-10^{14}cm^{-2}. Regardless of gas parameters, CN/HCN column density ratio is 1-10. This result can be reproduced by providing an additional UV radiation source of 0.001 to 0.044 G_0.
Conclusions. The UV radiation field is significantly higher in the closest distances from protostars. The astrochemical model shows that an additional source of UV radiation is needed to cover the abundances range indicated by observations.

Key words. astrochemistry – stars: formation – ISM: molecules – ISM: individual objects: Serpens Main – Submillimeter: ISM

1. Introduction

Low-mass stars are the most numerous objects among stellar population in galaxies (Kroupa 2002). At first stages of star formation protostars are formed inside molecular cloud, surrounded by massive envelopes exceeding for 10^4 AU in diameter (Lada 1987; Larson 2003; Bergin & Tafalla 2007). The embedded phases of low-mass star formation (Class 0/I YSOs, Andre et al. 1993) is characterised by gas and dust accretion from an envelope and bipolar, collimated outflows which carry out molecular gas from the dense core (Zuckerman et al. 1976, Arce & Sargent 2006).

The Serpens star forming cloud is one of the most active sources containing low-mass protostars within 500 pc (Evans et al. 2009). The latest distance estimations based on astrometric observations (Ortiz-León et al. 2017) place the cloud at 436±9 pc away. The cloud was selected as one of the target sources in the Spitzer Space Telescope Legacy project 'From Molecular Cores to Planet-forming Disks' (Evans et al. 2003) and the Herschel Gould belt survey (André et al. 2010). The first survey provided embedded sources identification based on

color-color diagrams (Harvey et al. 2007 and detailed calculation of bolometric luminosities, temperatures, and envelope masses (Enoch et al. 2009), as well as the catalog of identified YSOs (Dunham et al. 2015). The second program aims to characterise luminosities, temperatures and density profiles of prestellar cores and Class 0 protostars, and determine core mass functions and protostar luminosity functions.

The cloud core (hereafter referred to as Serpens Main) has been found in far-infrared and submillimeter observations as a dense area with several deeply embedded protostars Class 0/I (Casali et al. 1993, Hurt & Barsony 1996, Testi & Sargent 1998). Molecular observations of CO rotational transitions revealed outflows connected with the protostars (Davis et al. 1999, Dionatos et al. 2010). Individual sources were probed with the Water in Star-Forming Regions with the Herschel Space Observatory (WISH) project (van Dishoeck et al. 2011) and the "Dust, Ice, and Gas in Time" (Green et al. 2013).

Tracing the physical and chemical processes dominated by UV radiation lead to better understanding of the protostellar evolution. Signatures of chemical tracers characteristic

of warmer regions were noticed in the Serpens Main region (McMullin et al. 2000, Yıldız et al. 2015). The large Spitzer and Herschel surveys brought new insights into physical properties of the gas around low-mass protostars. Herschel-PACS observations of the high-J CO emission around low-mass protostars including Ser-SMM1, Ser-SMM3 and Ser-SMM4 showed the presence of a warm component about $T_{rot} \approx 300$ K, hot component of $T_{rot} \approx 600 - 800$ K (Karska et al. 2013, Green et al. 2013) and very hot component exceeding 1000 K for some sources (Manoj et al. 2013). The high-temperature CO emission can be explained as shocked-heated gas created by UV-irradiated shocks (Kristensen et al. 2017). Shock waves are created in the inner part of accretion disk where the gas is heated by the 10,000 K radiation filed (Spaans et al. 1995). UV photons propagate in low-density outflow cavities for large distances, modifying the chemical composition of low-mass protostars neighbourhood.

Previous studies of energetic processes around low-mass protostars showed observational premises of the influence of UV radiation on molecules. Higher emission of [C I] was observed at protostars positions than in off-source positions what brought to conclusion of photodissociation CO (van Kempen et al. 2009). The fluxes of [OI] and [CII] are significantly higher than fully-shielded C-shock models (Karska et al. 2018). The other photodissociation tracer H_2O/OH showed a few order of magnitude disagreement with shock models (Karska et al. 2014). Therefore, ultraviolet radiation may play an important role in low-mass protostars surroundings.

The relative abundance of CN and HCN molecules is widely used a tracer of UV radiation in different astronomical context: reflection nebulae (e.g. Fuente et al. 1995), proto-planetary disks (e.g. Chapillon et al. 2012), proto-brown dwarfs (e.g. Riaz et al. 2018). CN is a product of photodissociation of HCN with the photodissociation rate of 1.64×10^{-9}. CN has smaller photodissociation rate of 5.19×10^{-10} (Heays et al. 2017), thus is not that sensitive for photodissociation as HCN. Since CN and HCN can be photodissociated selectively, therefore the CN/HCN ratio probes regions affected by UV radiation. The ratio is the highest near the source of the UV emission, and decreases with the distance from the source (Fuente et al. 1993). We propose to use CN and HCN molecules as a tracer of UV radiation field around low-mass protostars.

Ultraviolet radiation can propagate in large scales of 1000 AU (Kristensen et al. 2017), changing the properties of the surrounding matter. Since the UV radiation around low-mass protostars was studied only in the source position (Stäuber et al. 2007, Riaz et al. 2018) or in the source closest neighbourhood (Hogerheijde et al. 1999, Bachiller et al. 2001, Jørgensen 2004), the spatial extend of UV fields in larger scales is the matter of question. We address the following questions in: How does the UV radiation affect the chemistry of the surrounding of the low-mass? If the molecules are dissociated in the inner envelope or in the outflows? What is the spatial extent of the UV fields from protostars and their outflows? What is the typical strength of UV radiation around Class 0/I protostars?

We present the CN, HCN, CS and their isotolopologues molecular data observed in the Serpens Main star forming region. Section 2 contains the overview of the observations and the targeted sample. The results derived from the observations are shown in the Section 3, while further analysis of the data in Section 4. In the section 5 we refer to the previous studies of the topic and provide the discussion of the results. The summarising Section 6 is closed with our conclusions.

2. Observations

2.1. IRAM data and reduction process

The Serpens Main star forming region was observed with IRAM 30 between 14 and 17 July 2009 (project no. xxx, PI: L. Kristensen). We used the Eight MIxer Receiver (EMIR) as the frontend. The observations were performed in the EMIR bands E090 (molecule HCN $J = 1 - 0$) covering the range 73-117 GHz and E150 (molecules CN $J = 1 - 0$ and CS $J = 3 - 2$) covering the frequencies between 125 and 184 GHz. Due to the EMIR receiver wide bands additional molecular lines of $C^{34}S$ $J = 3 - 2$, $H^{13}CN$ $J = 1 - 0$ and $H^{13}CN$ $J = 2 - 1$ were also observed. The backend was the Versatile SPectrometer Array (VESPA) autocorrelator and the 1 MHz filterbank reaching the spectral resolution of 39 kHz (E150 band) and 78 kHz (E090 band). The telescope beam size varies from 14″ at 172.68 GHz to 29″ at 86.34 GHz (Table 1). The antenna temperatures were converted to main-beam brightness temperature T_{MB} using the main beam efficiency according to the expresion: $T_{MB} = T_A/\eta_{MB}$. The exact upper levels enegies, line frequencies, beam sizes and beam efficiencies are given in Table 1. Observations included scans of the Ser-SMM1 (centered at $\alpha_{J2000} = 18^h29^m49.6^s$, $\delta_{J2000} = +01°15'20.5''$ with $V_{LSR} = +8.5$ km/s) and the Ser-SMM3/Ser-SMM4 (centered at $\alpha_{J2000} = 18^h29^m56.6^s$, $\delta_{J2000} = +01°14'00.3''$ with $V_{LSR} = +7.6$ km/s) regions, both 1′×3′ OTF maps. The size of the maps is about 300″ × 350″, covering both Ser-SMM1 and Ser-SMM3/Ser-SMM4 regions. The regions are referenced in the article as 'the Northen part' and 'the Southern part' respectively.

Data reduction was carried out with the CLASS package within GILDAS[1]. Each spectrum was corrected for the baseline shape, the spike channels were removed and the velocity was resampled to a resolution of 0.5 km/s. The baseline fitting of the order of 0 was sufficient for our observations. The rms of extracted spectra values vary from 0.024 K to 0.125 K. Both OTF maps were merged in one map covering 300×350 arcsec. The spectra obtained were exported from the CLASS package and analysed with Python scripts.

2.2. Physical properties of embedded protostars

Ten Class 0/I protostars are present in the observed region. There are deeply embedded sources so the radiation coming from theirs neighbourhood is highly absorbed in the envelopes, then re-emitted in the IR range. Envelopes become thinner with time due to outflow-envelope interactions (Arce & Sargent 2006). Class I sources SEDs are dominated by the emission in shorter wavelengths in respect to Class 0 objects. Thus Spectral Energy Distributions (SEDs) allow to estimate the evolutional stage of an object (Andre et al. 1993).

Figure A.1 shows spectral energy distributions for all Class 0/1 protostars in the region (Table 2). The SED plots include the selected literature samples (Dunham et al. 2015) combined with the data from the Herschel Gould Belt survey project (André et al. 2010). The additional Herschel data cover the SED peak, therefore provide a more detailed information allowing to calculate the bolometric temperatures and luminosities of the protostar more precisely.

Table 2 contains the observed protostars parameters as well as the classification from Enoch et al. 2009. Early Class 0 was defined as a protostar of bolometric temperature lesser than 50 K. Prostostars characterised by bolometric temperature between

---

[1] See http://www.iram.fr/IRAMFR/GILDAS

Table 1: Overview of the observations

Mol.	Trans.	ν (GHz)	E_u/k_B (K)	A_{ul} (s^{-1})	g_u	n_{crit} (cm^{-3})	Beam size ('')	Beam eff. η_{MB}
HCN	1-0	88.631602	4.25	2.407×10^{-5}	3	5.0×10^{6} [b]	28	0.81
CN	1-0	113.494921	5.45	1.182×10^{-5}	3	1.1×10^{5} [c]	22	0.78
CS	3-2	146.969029	14.1	6.071×10^{-5}	7	2.6×10^{5} [c]	16	0.74
C^{34}S	3-2	144.617109	13.9	7.251×10^{-5} [a]	7	7.3×10^{5} [a]	16	0.74
H^{13}CN	1-0	86.342274	4.14	1.512×10^{-5} [a]	3	9.7×10^{6} [b]	29	0.81
H^{13}CN	2-1	172.677881	12.43	6.90×10^{-5} [a]	5	1.2×10^{6} [c]	14	0.68

References: Molecular data adopted from LAMDA/JPL databases: [a] calculated for T = 300 K; [b]Jiménez-Donaire et al. 2016, assuming optically thin transition lines for an excitation temperature of 20K; [c]Shirley 2015, assuming optically thin transition lines for an excitation temperature of 50K; [d]Chandra et al. 1995.
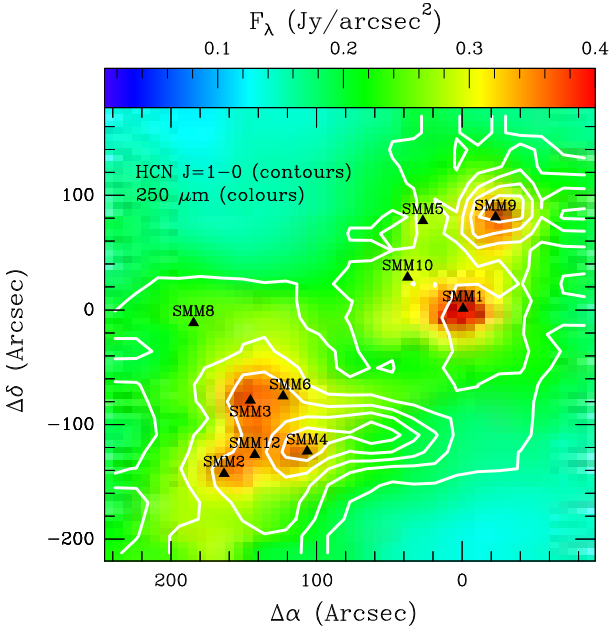
Notes. Beam sizes and efficiencies are taken from http://www.iram.es/IRAMES/mainWiki/Iram30mEfficiencies

Fig. 1: Molecular emission of HCN J=1-0 (contours) overplot on continuum emission *Herschel*/SPIRE (Griffin et al. 2010) 250 μm (colours). Countours the lowest level is set on 0.4 K km/s (30 σ), step size of 4 K km/s.

50 K and 100 K were classified as Late Class 0 protostars. Class I protostars were divided for Early and Late sub-type by the bolometric temperature of 300 K.

Most of the observed protostars in the Serpens Main region are very young, embedded sources of Early Class 0. SMM4, SMM10 and SMM12 are classified as Late Class 0 YSOs. The SMM5 and SMM6 protostars are the most evolved objects in our sample (Class I).

3. Results

3.1. Molecular emission maps

The line maps in the targeted molecules show variety of structures that can be associated with YSOs and a large-scale cloud emission. Different spatial extend in molecules radiation is connected with various physical conditions around protostars. Here, we present the large-scale maps of CS $J = 3 - 2$, HCN $J = 1 - 0$

and CN $J = 1 - 0$. Maps of their isotopologues are shown in the Appendix A.

We present large-scale intensity maps (Fig. 2) of the targeted lines integrated at the level of 3 σ and above. Three of the observed molecules (HCN, CN and H^{13}CN) are characterised by hyperfine structure. High resolution spectroscopy allow us to separate the emission from each hyperfine transitions. The integrated intensity maps of the lowest transitions of HCN, CN and H^{13}CN are performed as a sum of all hyperfine splitting components. The maps are centred at α_{J2000} = 18^{h}29^{m}46.6^s, δ_{J2000} = 01°18′20.5″.

Most of molecular emission is concentrated in the SE subcluster, where 6 low-mass protostars are located, while the continuum emission peaks in the NW subcluster what is correlated with the other 4 low-mass protostars positions. The most extended structures can be associated with molecular outflows ejected from low-mass protostars (Table 2). Outflows directions were marked based on previous studies in CO transitions CO $J = 3 - 2$ (Dionatos et al. 2010) and CO $J = 6 - 5$/CO $J = 3 - 2$ (Yıldız et al. 2015). Five off-source positions were selected to detailed spectra analysis (Table 3).

The integrated line intensity map of HCN $J = 1 - 0$ shows extended emission along outflow directions. This is the strongest line among all observed. The emission is slightly correlated with continuum emission. Most of the emission is associated with protostars positions. The HCN $J = 1 - 0$ gas peaks around Ser-SMM9 and Ser-SMM4 protostars. There is no significant peak around strong submillimetre sources as Ser-SMM1 and Ser-SMM3. The low energy level of HCN ($E_u = 4.25$ K) with the critical density of 10^6 cm^{-2} traces cold, high-density gas. HCN has previously been shown to be a good tracer of molecular outflows activity (Lee et al. 2014). The HCN $J = 1 - 0$ line was detected at all protostars positions, although it is weak at the positions of Ser-SMM5, Ser-SMM8 and Ser-SMM10. On the other hand, the HCN $J = 1 - 0$ emission is particularly strong in Ser-SMM4 blue-shifted outflow (outflow position no. 4). In NS elongated structure is present around Ser-SMM1 protostar what was noticed also in high-J CO transitions (Yıldız et al. 2015). The emission is slightly extended along Ser-SMM9 outflows. There is no intensively elongated outflow structure from the other sources.

CS $J = 3 - 2$ line emission map shows similar spatial distribution to HCN $J = 1 - 0$. Both species trace the gas of the same properties, however the CS molecule is excited in slightly less dense environment ($\sim 10^5$ cm^{-3}). The most significant elongated
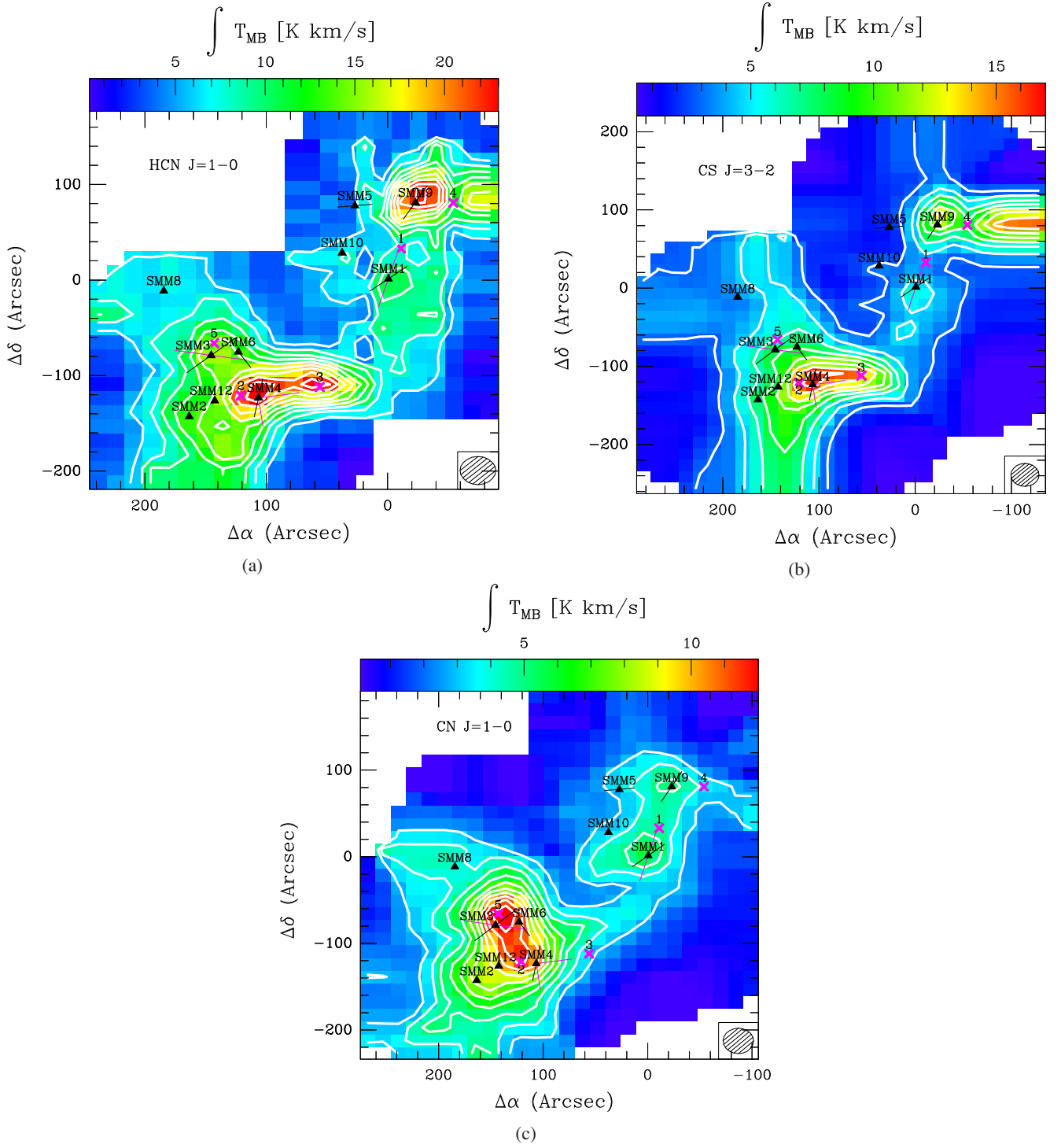
Fig. 2: Integrated intensity $\int T_{\mathrm{mb}}\, dV$ of the HCN $J = 1 - 0$ (upper left panel), CS $J = 3 - 2$ (upper right panel) and CN $J = 1 - 0$ (bottom panel) in the Serpens Main region. The first contour at 30 σ level, with step of 10 σ, except CS $J = 3 - 2$ line (b) where the first contour is at 10 σ with step of 5 σ. Black triangles show the positions of the protostars (Suresh et al. 2016), whereas the black lines (Yıldız et al. 2015) and magneta line (Dionatos et al. 2010) show the associated outflow directions. Outflow positions are displayed as magneta crosses.

structure can be associated with Ser-SMM4 blue-shifted outflow. It is situated at the same place in both maps, extending over 80″. A similar large-scale structure is detected along Ser-SMM1 outflows, although it is stronger in the HCN $J = 1-0$ map. Emission around Ser-SMM9 have a circular shape, however, there is additional elongated structure in CS $J = 3 - 2$ line emission towards

the West. It overlaps with the S68N outflows seen in methanol observations (Kristensen et al. 2010). The HCN $J = 1 - 0$ line emission propagates for larger distances than the CS $J = 3 - 2$. It is also relatively stronger. In both cases the highest peak of the emission is situated around Ser-SMM4 protostar with a significant extent towards outflow position no. 3. Their weaker isotopic

Table 2: Catalogue of protostars properties

Source	R.A. (J2000.0)	Decl. (J2000.0)	T_{bol} (K)	L_{bol} ($L_\odot$)	Class	Other names
SMM9	18 29 48.3	+01 16 42.7	34.9	10.3	Early Class 0	Ser-emb8, ISO241, WMW23, Bolo22
SMM1	18 29 50.0	+01 15 20.3	35.4	78.7	Early Class 0	Ser-emb6, FIRS1, EC41, Bolo23
SMM5	18 29 51.4	+01 16 38.3	150.5	3.7	Early Class I	Ser-emb21, EC53, WMW24, Bolo22
SMM10	18 29 52.3	+01 15 48.8	82.6	6.2	Late Class 0	Ser-emb12, WMW21, Bolo 23
SMM4	18 29 57.0	+01 13 11.3	76.9	4.4	Late Class 0	Ser-emb22, Bolo25
SMM6	18 29 57.8	+01 14 05.3	532.3	43.1	Late Class I	Ser-emb30, EC90, WMW35, SVS20S, Bolo 28
SMM12	18 29 59.1	+01 13 14.3	96.9	5.7	Late Class 0	Ser-emb19, Bolo28
SMM3	18 29 59.6	+01 13 59.2	35.0	6.9	Early Class 0	Ser-emb26, Bolo26
SMM2	18 30 00.5	+01 12 57.8	30.5	4.07	Early Class 0	Ser-emb4, Bolo28
SMM8	18 30 01.9	+01 15 09.2	15.3	0.2	Early Class 0	Bolo30

Coordinates taken from Suresh et al. 2016, except SMM8 (Lee et al. 2014).

Table 3: Properties of the selected off-source positions

Pos.	R.A. (J200)	Decl. (J200)	Remarks
1	18:29:45.47	+01:15:53.5	SMM1 blue-shifted outflow in CO $J = 3 - 2$
2	18:29:54.66	+01:13:19.5	max. CN $J = 1 - 0$, SMM4 blue-shifted outflow in CO $J = 3 - 2$
3	18:29:50.33	+01:13:68.5	max. HCN $J = 1 - 0$, SMM4 blue-shifted
4	18:29:43	+01:16:41.5	outflow visible in C^{34}S(3-2)
5	18:29:56.13	+01:14:14.5	max. CN $J = 1 - 0$, SMM9 surroundings

Fig. 3: Integrated intensity $\int T_{mb}\, dV$ of CN $J = 1 - 0$ (colours) and HCN $J = 1 - 0$ (contours) in the Serpens Main region. The first contour is 30. Triangles and lines marked as decribed in 2.

species H^{13}CN $J = 1 - 0$ and C^{34}S(3-2) lines peak around the protostars position. The lines exhibits similar morphological distribution as HCN $J = 1 - 0$ and CS $J = 3 - 2$.

CN $J = 1 - 0$ line emission is focused mostly around the positions of protostars. The CN line is similarly low-energetic, however it peaks in different areas than HCN and CS. The CN $J = 1 - 0$ integrated intensity structures follow the 250 μm continuum map. The highest local peaks are associated with Class 0 low-mass protostars: Ser-SMM3, Ser-SMM4 and Ser-SMM6, as well as local maxima around Ser-SMM1 and Ser-SMM9. The spatial distribution is qualitatively different compared to the HCN $J = 1 - 0$ and CS $J = 3 - 2$ maps. The strongest emission characterises the dense surroundings of protostars in SE subcluster while the NW subcluster does not show such a distinct emission as in the HCN $J = 1 - 0$ line. Dense emissive region of the Ser-SMM9 source is significantly weaker in CN $J = 1 - 0$ line. CN $J = 1 - 0$ map can be characterised by compact, condensed emission without any strongly elongated structures.

3.2. Comparison of the spatial extent of CN and HCN

We present a large-scale map of CN $J = 1 - 0$ and HCN $J = 1 - 0$ integrated intensity (Fig. 3) showing the emission exceeding 30 σ for both molecules. The image of CN emission has been resampled to beam size of HCN in order to compare the same emitting regions.

The CN $J = 1 - 0$ transition is shifted to the north in respect to the HCN $J = 1 - 0$ emission. It is highly concentrated in the SE subcluster, while the NW subcluster is dominated ny the HCN. Both molecules show a diffusive 'bridge' between the two subclusters. It is connected with Ser-SMM4 and Ser-SMM1 outflows in HCN, while the CN follows the dust continuum emission. The emission in both molecules is anti-corelated north from Ser-SMM6 and west from Ser-SMM4 sources. At the dense area of Ser-SMM9 surrounding CN/HCN ratio is significantly weaker.

Both species has been detected in all sources positions. CN as a product of HCN photodissotiation indicates other properties of low-mass protostars surroundings (Section 4). The highest CN/HCN integrated intensity ratio occurs in Ser-SMM6 and Ser-SMM3 protostars, as well as in the outflow position no. 5. On the other hand, Ser-SMM9 object is characterised by very low CN/HCN line ratio. Similarly low CN/HCN ratio is measured in outflow positions no. 3 and 4.
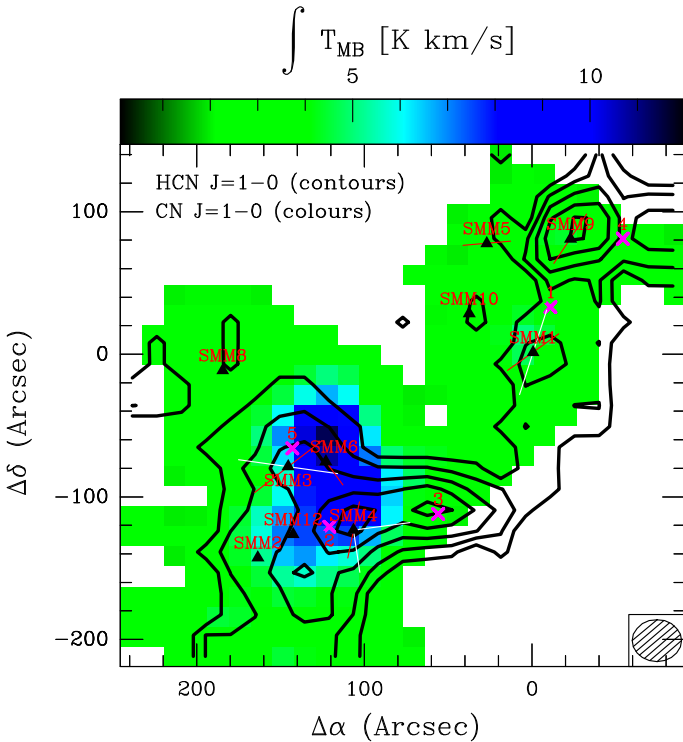
Table 4: CN/HCN integrated intensities

Source	$\int T_{\mathrm{mb}}\,dV\mid_{CN}$ (K km/s)	$\int T_{\mathrm{mb}}\,dV\mid_{HCN}$ (K km/s)	CN/HCN
SMM1	5.26	8.23	0.64
SMM2	8.41	12.57	0.67
SMM3	13.18	14.14	0.93
SMM4	9.89	17.59	0.56
SMM5	3.49	5.79	0.60
SMM6	10.57	11.85	0.89
SMM8	5.09	6.32	0.81
SMM9	5.41	14.08	0.38
SMM10	2.59	6.96	0.37
SMM12	9.10	13.27	0.69
Outflow1	4.8	8.3	0.58
Outflow2	11.2	21.4	0.52
Outflow3	3.8	23.6	0.16
Outflow4	3.7	12.4	0.3
Outflow5	13.3	14.9	0.89

Most of the sources show high flux values in both molecules (Table 4). However, they present unequal levels which indicates regions of different properties. In order to better understand this issue we analyse the molecular line profiles in the Section 3.2.

3.3. Line profiles

We selected 14 representative on-source and off-source positions for a detailed analysis (Fig. **??**). Nine of them are corresponding to the protostars positions, the other five off-source positions were selected based on local maximum of the flux.

In the majority of our sources five of targeted lines were detected: CN $J = 1 - 0$, HCN $J = 1 - 0$, CS $J = 3 - 2$, $C^{34}S$ $J = 3 - 2$ and $H^{13}CN$ $J = 1 - 0$. The line is considered to be detected if there is an emission at the level of at least 3σ. A weak emission from $H^{13}CN$ $J = 2 - 1$ was found at the positions of four sources and it is not included in Fig. **??**.

The strongest emission occurs in HCN $J = 1 - 0$, CN $J = 1 - 0$ and CS $J = 3 - 2$ lines and it was detected at the position of all of the sources. The emission in the other lines was multiplied in order to compare profiles between different molecules. In HCN, CN species and their isotopologues a few different velocity components can be identified what indicates the hyperfine splitting. This occurs if a molecule has a non-zero nuclear spin so there is also an interaction between the nuclear spin and the electronic angular momentum. The most distinct splitting can be spotted in the CN $J = 1 - 0$ profiles with five separate components situated between -70 km/s and 18 km/s. The HCN $J = 1 - 0$ line is characterised by three components with low separation situated in the range of -2 km/s – 16 km/s.

Ser-SMM1, Ser-SMM9, and Ser-SMM10 sources have wide spectral lines, while others exhibit narrow line profiles. Spectra extracted form Outflows no. 1, 4 and 5 shows prominent blue-shifted wings. Similar structure can be noticed in the Ser-SMM3 (panel no. 7) CS 3-2 and HCN $J = 1 - 0$ profiles.

3.4. Opacity

HCN has a high critical density and it is relatively abundant molecule. Thus, it is a good density tracer, typically thick in low-J transitions. Usually molecules with hyperfine splitting observed are used to probe the optical depth, but the HCN

show anomalies in the hyperfine splitting. Therefore, a standard method of estimating the optical depth from the ratio of lines from two isotopologues (Goldsmith et al. 1984) was applied to HCN observations. Assuming that both HCN and $H^{13}CN$ are in LTE at the same excitation temperature and the $H^{13}CN$ is optically thin (Hogerheijde et al. 1999), the optical depth can be determined from the ratio of brightness temperatures and abundances:

$$\frac{T_{\mathrm{HCN}}}{T_{\mathrm{H^{13}CN}}} = \frac{X[\mathrm{HCN}]}{X[\mathrm{H^{13}CN}]}\frac{1 - \exp(-\tau_{\mathrm{HCN}})}{\tau_{\mathrm{HCN}}} \tag{1}$$

The HCN/$H^{13}CN$ abundance ratio was estimated at 30 (Daniel et al. 2013). The optical depth calculated for all the protostars positions varies from 2 to 7.6 what is consistent with RADEX outputs assuming the column density of HCN as 3×10^{14} cm^{-2}, hydrogen density as 10^5 cm^{-3} and kinetic temperature of the gas as 50 K.

Similar RADEX calculations were performed for CN molecule. Assuming the same gas conditions and slightly higher column density of 10^{15} cm^{-2}, we obtained comparable results.

It is seen that both the HCN and CN lines are optically thick so the calculated column densities can be underestimated by up the order of magnitude. Nevertheless, while both lines are similarly thick, this will have little effect on the relative values of calculated column densities.

4. Analysis

4.1. Lines column densities

Table 5 shows fluxes integrated from the average line profile at the positions of known protostars. Flux calculation in individual lines allows us to determine the column density of a given transition. The column density of the upper level N_{up} of each observed line was calculated based on following relation:

$$N_u = \beta\,\frac{\nu\,W}{A} \tag{2}$$

where $\beta = 1937$ cm^{-2} and $W = \int T_{mb}\,dV$ is the integrated intensity of the emission line. The frequency ν should be given in GHz. The total column density was obtained using:

$$N_{tot} = Q(T_{ex})\,\exp(\frac{E_u}{k\,T_{ex}})\frac{N_u}{g_u} \tag{3}$$

where is the partition function depending on excitation temperature T_{ex} and k Boltzmann constant.

The column densities of the upper level of CN $J = 1 - 0$ and HCN $J = 1 - 0$ transitions are presented in Table 5. The lowest transition of CN is more abundant molecule than the lowest transition line of HCN at the low-mass protostars positions. The column density of CN $J = 1 - 0$ varies between 10^{14} -10^{15} cm^{-2}, while in the column density of the HCN's lowest transition reaches 10^{14} cm^{-2}. In the case of Ser-SMM2, Ser-SMM3, Ser-SMM4, Ser-SMM6 and Ser-SMM12 HCN $J = 1 - 0$ line column density is an order of magnitude lower than the column density of the equivalent CN transition. This result provides a clue to better understand of the low-mass protostars chemistry.

4.2. RADEX modelling

Column densities can be independently determined using molecular excitation models. Line ratio can provide additional information concerning physical properties of the observed gas.
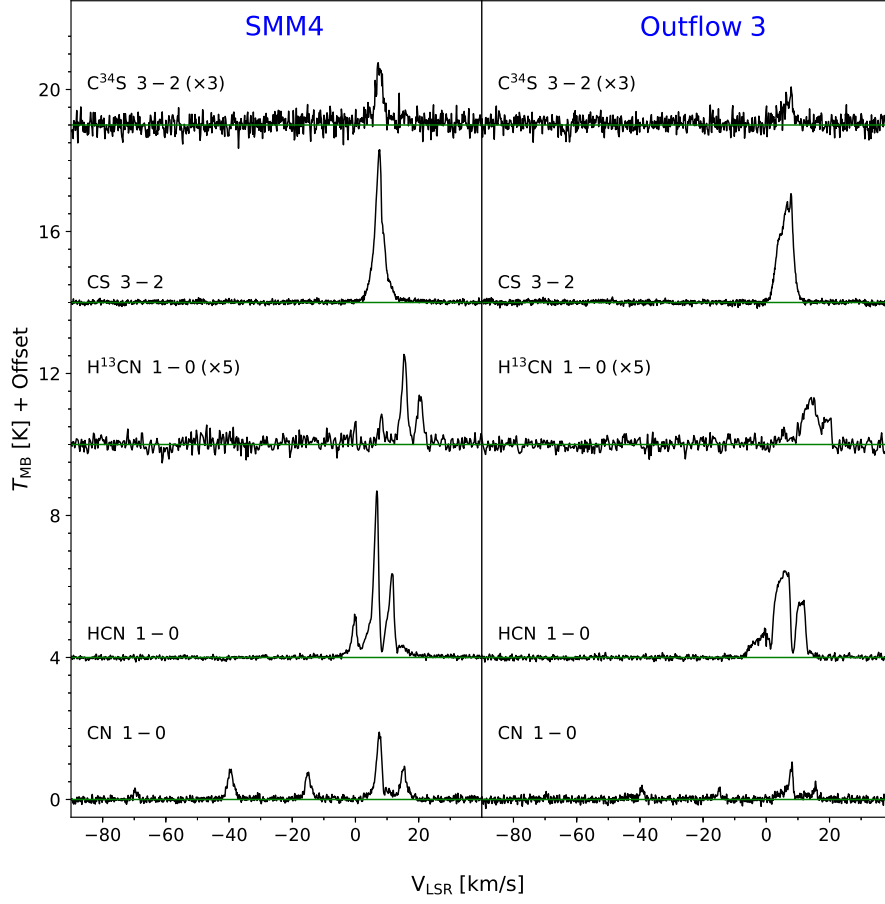
Fig. 4: Spectra of $C^{34}S$ $J = 3 - 2$, CS $J = 3 - 2$, $H^{13}CN$ $J = 1 - 0$, HCN $J = 1 - 0$ and CN $J = 1 - 0$ lines obtained in a protostar position (left) and an outflow position (right).
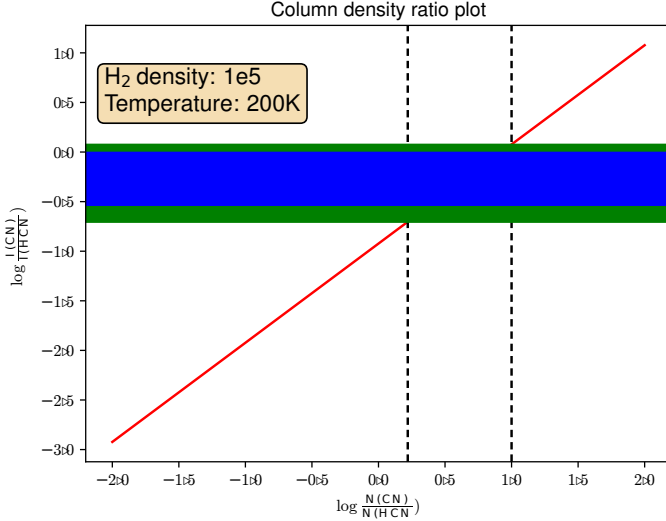

Fig. 5: CN/HCN column density ratio for hydrogen densities of $n_{H_2} = 10^5$ cm^{-3} and kinetic temperatures of $T_{kin} = 200$ K (red line). The observed line intensity ratio is plotted in blue (protostars positions) and green (all positions).

Using non-LTE radiative transfer code RADEX (van der Tak et al. 2007) we have prepared sets of molecular excitation models. Assuming the excitation conditions of the CN J=1-0 and HCN J=1-0 lines, their column densities ratio may be estimated. In order to ensure optically thin emission, HCN column density was set as 10^8 cm^{-2}. In our models CN column density parameter varies from 10^6 cm^{-2} to 10^{10} cm^{-2}. These translates into N_{CN}/N_{HCN} in following limits: 10^{-2}-10^2.

The sets of models were obtained assuming a line width of 1.0 km s^{-1}, 2.73 K of background radiation and spherical geometry. Each set of models varies with the following input parameters: hydrogen densities ranged from $n_{H_2} = 10^3$ cm^{-3} to $n_{H_2} = 10^5$ cm^{-3} and kinetic temperatures of $T_{kin} = 30$ K, $T_{kin} = 75$ K and $T_{kin} = 200$ K. The molecular data files used during modelling were procured from the Leiden Atomic and Molecular Database (LAMDA, Schöier et al. 2005). For each sets of models CN/HCN column density ratio and the the observational constraints of CN/HCN integrated intensities ratio were the only free parameters.

Fig. 5 presents one exemplary set of models of CN/HCN column density ratio versus the modelled line intensities ratio for hydrogen densities of $n_{H_2} = 10^5$ cm^{-3} and kinetic temperatures of $T_{kin} = 200$ K. The rest of the models are shown in the Appendix B. The modelled line intensities are compared with the observations. The best fit of the observed line intensity ratio covers a range of 0.0-1.0 of the column density ratio in the logarithmic scale. That corresponds to a few times higher CN column density than the same parameter of HCN. CN/HCN column density ratio weakly depends on hydrogen density and kinetic temperature in the low limit of those parameters (see Table 6).

Table 5: Integrated fluxes of the observed line at the positions of protostars

Source	Line	$\int T_{mb}\,dV$ (K km/s)	T_{peak} (K)	N_{up} (cm^{-2})	N_{tot} (cm^{-2})
SMM1	CN 1-0	5.26	0.89	1.1×10^{13}	6.6×10^{14}
	HCN 1-0	8.23	1.76	5.2×10^{12}	2.0×10^{14}
	CS 3-2	2.98	1.57	2.1×10^{12}	2.3×10^{13}
	C^{34}S 3-2	1.21	0.56		
	H^{13}CN 1-0	1.43	0.45		
SMM2	CN 1-0	8.41	1.92	1.8×10^{13}	1.1×10^{15}
	HCN 1-0	12.57	3.48	8.0×10^{12}	3.0×10^{14}
	CS 3-2	6.57	3.10	4.5×10^{12}	2.0×10^{13}
	C^{34}S 3-2	0.89	0.47		
	H^{13}CN 1-0	1.65	0.64		
SMM3	CN 1-0	13.18	3.42	2.8×10^{13}	1.7×10^{15}
	HCN 1-0	14.14	4.95	8.9×10^{12}	3.4×10^{14}
	CS 3-2	8.11	2.90	5.6×10^{13}	6.2×10^{13}
	C^{34}S 3-2	0.60	0.36		
	H^{13}CN 1-0	0.88	0.41		
SMM4	CN 1-0	9.89	1.90	2.1×10^{13}	1.3×10^{15}
	HCN 1-0	17.59	4.69	1.1×10^{13}	4.2×10^{14}
	CS 3-2	14.4	4.30	9.9×10^{12}	1.1×10^{14}
	C^{34}S 3-2	1.56	0.64		
	H^{13}CN 1-0	1.83	0.61		
SMM5	CN 1-0	3.49	0.94	7.3×10^{12}	4.4×10^{14}
	HCN 1-0	5.79	1.72	3.7×10^{12}	1.4×10^{14}
	CS 3-2	2.61	1.48	1.8×10^{12}	2.0×10^{13}
	C^{34}S 3-2	0.28	0.42		
	H^{13}CN 1-0	1.16	0.42		
SMM6	CN 1-0	10.57	3.17	2.2×10^{13}	1.3×10^{15}
	HCN 1-0	11.85	5.15	8.9×10^{12}	3.3×10^{14}
	CS 3-2	7.86	3.2	5.4×10^{12}	6.0×10^{13}
	C^{34}S 3-2	0.74	0.56		
	H^{13}CN 1-0	0.81	0.40		
SMM8	CN 1-0	5.09	0.94	1.1×10^{13}	6.4×10^{14}
	HCN 1-0	6.32	1.72	4.0×10^{12}	1.5×10^{14}
	CS 3-2	4.64	2.08	3.2×10^{12}	3.5×10^{13}
	C^{34}S 3-2	0.22	0.35		
	H^{13}CN 1-0	0.46	0.21		
SMM9	CN 1-0	5.41	0.84	1.1×10^{13}	6.8×10^{14}
	HCN 1-0	14.08	2.40	8.9×10^{12}	3.4×10^{14}
	CS 3-2	9.85	2.70	6.8×10^{12}	7.5×10^{13}
	C^{34}S 3-2	1.3	0.62		
	H^{13}CN 1-0	1.57	0.38		
SMM10	CN 1-0	2.59	0.78	5.4×10^{12}	3.3×10^{14}
	HCN 1-0	6.96	1.75	4.4×10^{12}	1.7×10^{14}
	CS 3-2	3.83	1.43	2.6×10^{12}	2.9×10^{13}
	C^{34}S 3-2	0.56	0.40		
	H^{13}CN 1-0	0.98	0.45		
SMM12	CN 1-0	9.10	1.85	1.9×10^{13}	1.2×10^{15}
	HCN 1-0	13.27	3.50	8.4×10^{12}	3.2×10^{14}
	CS 3-2	9.75	3.26	6.7×10^{12}	7.4×10^{13}
	C^{34}S 3-2	1.18	0.58		
	H^{13}CN 1-0	1.43	0.46		

The sets of models shown in this section indicate that CN/HCN column density ratio covers the range of 1-10 regardless of excitation conditions.

Table 6: CN/HCN column density ratio

n_{H_2} (cm^{-3})	T_{kin} (K)	$\log_{10}(N[CN]/N[HCN])$
10^3	30	0.03-0.88
10^3	75	0.06-0.84
10^3	200	0.00-0.78
10^4	30	0.16-0.94
10^4	75	0.08-0.86
10^4	200	0.04-0.82
10^5	30	0.20-0.98
10^5	75	0.18-0.86
10^5	200	0.22-1.00

5. Discussion

5.1. Astrochemical model

In Section 3.2 we raised a question about influence of the UV radiation on the surroundings of the observed sources. We used the Nahoon astrochemical model in order to estimate the intensity of the UV field in reference to units of the interstellar UV field G_0.

The Nahoon is a numerical code allowing to determine the gas-phase chemistry in astrononomical context (Wakelam et al. 2012). The solver computes the chemical evolution in time of 489 species involving 6992 gas-phase and gas-grain reactions based on rate coefficients stored in the Kinetic Database for Astrochemistry (KIDA)[2]. The Nahoon code can model chemistry at a fixed temperature and density (0D modeling), as well as at grid of temperature, density and visual extinction (1D modeling). The UV radiation is described through the relation between visual extinction A_V and the photodissociation rate coefficient k Eq 4:

$$k = \alpha e^{-\gamma A_V} \tag{4}$$

Here, α and γ are coefficients of photodissociation of HCN equal to 1.64×10^{-9} and 3.12 respectively (Heays et al. (2017)). All models were performed at the 1D modeling grid with the latest version of Nahoon code (Nahoon_kida.uva.2014).

The evolution of the chemical network was started at the time of a dense cloud formation. Figure 6) shows a model corresponding to a typical dense cloud with temperature of 10 K and hydrogen total density of $n_{HI+2H_2} = 10^4$ cm^{-3}. The chemical composition of the CN, HCN and CS molecules stabilises at the time of 10^7 yrs with HCN abundance higher compared to CN. We assumed the time of 10^6 yrs as the time when the star formation starts in dense clouds. The modelled abundances of the all 489 species at the time of 10^6 yrs were used as an input data for the following set of models.

The closest neighbourhood of low-mass protostars was simulated based on the initial abundances of all species from starless cloud modelling. We adopted the UV radiation and cosmic ray fluxes typical for dense clouds as an initial conditions. The visual extinction and the total cosmic-ray ionization rate were set to 5 mag and 1.3×10^{17} s^{-1} respectively. The sets of models were run for the temperature range between 10 and 200 K and the total hydrogen densities from 10^4 cm^{-3} to 10^6 cm^{-3}. The results (Fig. 7) are consistent with starless cloud model. Without any additional source of the UV radiation HCN is more abundant than CN by about 2-3 orders of magnitude. Moreover, the model

[2] http://kida.obs.u-bordeaux1.fr/
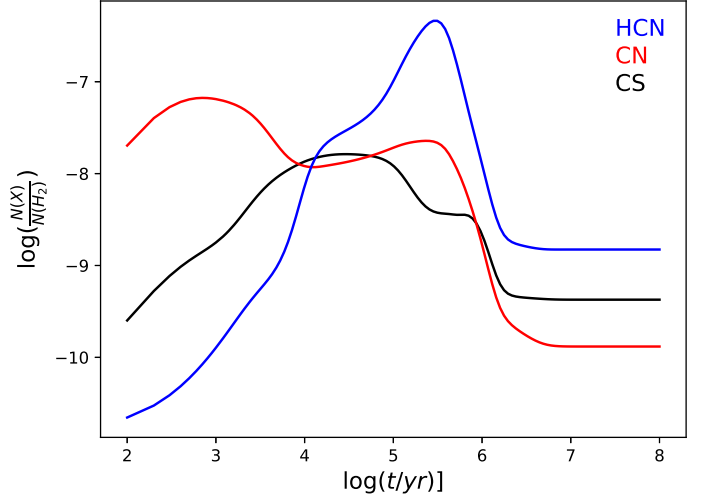
Fig. 6: Time evolution of CN (red line), HCN (blue line) and CS (black line) abundances obtained with Nohoon astrochemical code with initial parameters of $n_{HI+2H_2} = 10^4$ cm^{-3}, $T = 10$ K, $A_V = 5$ mag. The assumed cosmic-ray ionization rate is 1.3×10^{17} s^{-1}, dust to gas mass ratio is 0.01, dust grain radius is 10^{-5} cm, grain density is 3 g cm^{-3}.
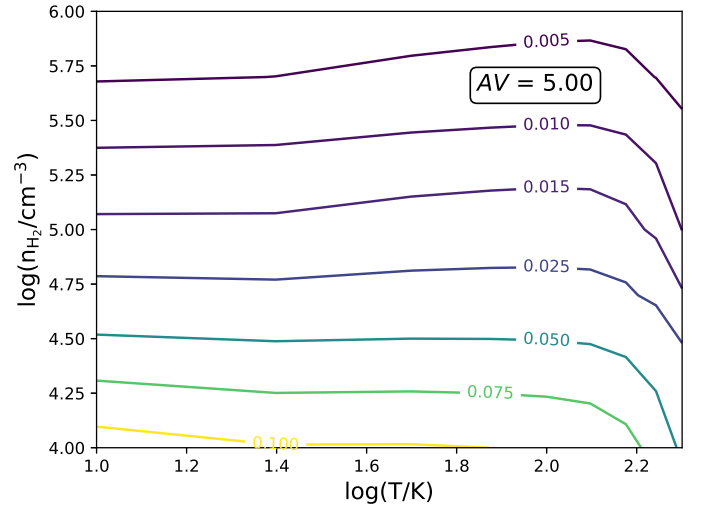

Fig. 7: Contour plot of Nahoon sets of models of CN/HCN abundances ratio with fixed visual extinction $A_V = 5$ mag at the time of 10^7 yrs after star formation began in the cloud.

shows that CN/HCN abundances ratio is slightly dependent on gas temperature up to 150 K.

These results justify assumptions for modelling the neighbourhood of low-mass protostars with the gas temperature of 50 K allowing to fix one of the model's parameters. The code was run for the range of visual extinction between -4.5^m and 2.5^m that corresponds to the UV radiation field G_0 of 4×10^{-4} to 1.25×10^6. The computed CN/HCN abundances ratio is presented in Fig. 8. The calculated column density ratio covers parameter space of all probed densities and G_0 range between 10^{-4} and 0.05 in weak UV radiation regime. The observed CN/HCN
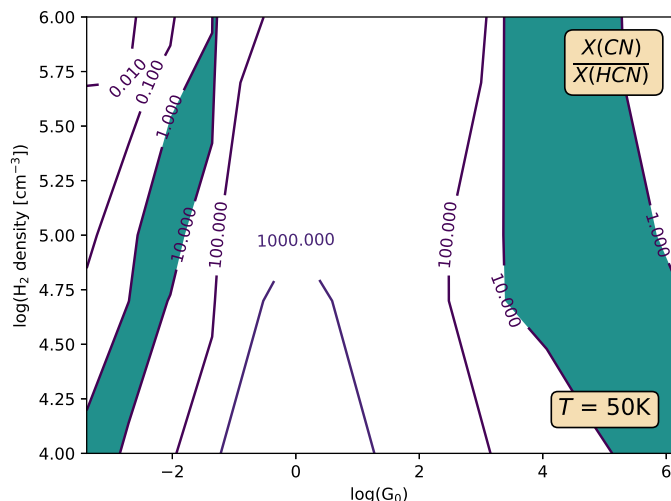
Fig. 8: Similar to Fig. 7 but for fixed temperature T = 50 K.

ratio is reproduced at the G_0 values greater than 1.5×10^3 as well. HCN is more abundant than CN in very weak ($<10^{-3}$ G_0) radiation fields. This result is consistent with simulations of a starless cloud that leads to a conclusion that additional UV radiation source is needed to reproduce the observational ratios.

Comparing CN/HCN results with similar plots of CN/CS and CS/HCN ratio (Fig. E.1 and Fig. E.2 respectively) restricts the parameter space to very low-density and weakly irradiated gas or a dense gas with strong UV radiation. CN/CS ratio varies between 9 and 29 for the all protostars positions, while CS/HCN ratio is in range of 0.12-0.26. Astrochemical models computed for these molecules show similar behaviour to that presented for CN/HCN ratio. UV radiation with the strength of G_0 in order of $10^3 - 10^4$ is not very probable in low-mass protostars neighbourhood. At the protostars' positions high hydrogen densities can be assumed. Astronomical models show that an additional UV radiation source of the strength of few hundredth of the average interstellar UV radiation field is required to cover the observational ratios.

Low CN/HCN ratio found in astrochemical model for strongly irradiated gas was a surprising result. Both production and destruction of each molecule need to be investigated in order to explain the reason behind HCN abundances being higher than expected. Detailed models of the most dominant reactions for destruction and production of each molecule are presented in Fig. F.1 – Fig. F.4 with the assumption of fixed 50 K temperature. Reaction flux is defined as reactants abundances multiplied by reaction rate coefficient. Only these reactions were taken into consideration which accumulated flux is greater than 80% of the total flux of all reactions contributed in the studied molecules destruction or production.

The reactions distribution in the parameter space is not very strongly depended on hydrogen densities. The strength of an additional UV radiation source is the parameter that distinguishes the dominant reactions the most. It was divided into three regimes: with weak, intermediate and strong UV field. The reactions where CN or HCN production or destruction is greater than 30% are listed in Tab. 7 as well as illustrated in Fig. F.5-Fig. F.7.

In the regime of weak UV radiation fields dominant formation channels of CN and HCN are hydrocarbons (CH and CH_2

respectively) reactions with atomic nitrogen. In more dense areas electron reaction with CNC cation plays role in the CN formation. The destruction of CN is mostly dominated with reaction with neutral oxygen (60-70%) or nitrogen (30% or less). In weakly irradiated environment atomic elements are more abundant in the neutral state. More of the ionised atoms are produced with the increase of the UV radiation what blocks these effective channels of CN destruction.

On the other hand, HCN destruction is driven by many channels in the weakest UV regime. Simultaneous impact of few different reactions is not as effective as the reaction ruling the CN destruction. It leads to higher HCN abundances compared to CN. HCN reaction with abundant C+ is the dominant destructive reaction for slightly stronger radiation fields ($>10^{-3}$). This reaction results in CNC+ production which quickly reacts with electron forming CN. That explains why CN/HCN ratio increases with larger radiation.

CN/HCN ratio is widely used as UV radiation tracer in PDRs (eg. Thi et al. 2004, Han et al. 2015). HCN photodissociates into CN molecule and H atom, while CN requires more energetic photon (> 12.4 eV) to be disintegrated (van Dishoeck 1987). This leads to higher abundance of CN molecules and increases CN/HCN column density ratio. Fluxes of HCN photodissociation (Fig. F.2) show that this reaction has marginal contribution in nitrogen chemistry up to $G_0 \approx 100$.

6. Conclusions

- HCN $J = 1-0$ and CN $J = 1-0$ show different spatial distribution. The emission of CN is concentrated at the positions of protostars, while HCN traces molecular outflows.
- CN/HCN column density ratio is in the range of 1-10 calculated both with LTE and non-LTE assumption.
- An additional source of UV radiation of the strength $G_0 \approx 10^{-2}$ is required to cover the observational CN/HCN range. There is non-zero UV radiation field around low-mass protostars.
- CN/HCN ratio starts to play important role in the nitrogen bearing spieces chemistry at $G_0 \approx 10^2$.

References

André, P., Men'shchikov, A., Bontemps, S., et al. 2010, A&A, 518, L102
Andre, P., Ward-Thompson, D., & Barsony, M. 1993, ApJ, 406, 122
Arce, H. G. & Sargent, A. I. 2006, ApJ, 646, 1070
Aso, Y., Hirano, N., Aikawa, Y., et al. 2018, ApJ, 863, 19
Bachiller, R., Pérez Gutiérrez, M., Kumar, M. S. N., & Tafalla, M. 2001, A&A, 372, 899
Bergin, E. A. & Tafalla, M. 2007, ARA&A, 45, 339
Casali, M. M., Eiroa, C., & Duncan, W. D. 1993, A&A, 275, 195
Chapillon, E., Guilloteau, S., Dutrey, A., Piétu, V., & Guélin, M. 2012, A&A, 537, A60
Daniel, F., Gérin, M., Roueff, E., et al. 2013, A&A, 560, A3
Davis, C. J., Matthews, H. E., Ray, T. P., Dent, W. R. F., & Richer, J. S. 1999, MNRAS, 309, 141
Di Francesco, J., Johnstone, D., Kirk, H., MacKenzie, T., & Ledwosinska, E. 2008, ApJS, 175, 277
Dionatos, O., Nisini, B., Codella, C., & Giannini, T. 2010, A&A, 523, A29
Dunham, M. M., Allen, L. E., Evans, Neal J., I., et al. 2015, ApJS, 220, 11

Table 7: Dominant processes in CN, HCN chemistry

Molecule	Weak UV fields $(G_0 = 10^{-3} - 10^{-1})$	Medium UV fields $(G_0 = 10^{-1} - 10^{1})$	Strong UV fields $(G_0 = 10^{1} - 10^{6})$
		Destruction	
CN	$O + CN \rightarrow N + CO$ $CN + N \rightarrow C + N_2$	$CN + ph \rightarrow C + N$ $O + CN \rightarrow N + CO$	$CN + ph \rightarrow C + N$
		Production	
	$N + CH \rightarrow H + CN$ $CNC^+ + e^- \rightarrow C + CN$ $N + C_2 \rightarrow C + CN$	$N + C_2 \rightarrow C + CN$ $H + CN^+ \rightarrow CN + H^+$	$HCN^+ + e^- \rightarrow H + CN$ $N + CH \rightarrow H + CN$ $H + CN^+ \rightarrow CN + H^+$ $N + C_2 \rightarrow C + CN$
		Destruction	
HCN	$HCN + C^+ \rightarrow H + CNC^+$ $HCN^+ + HCO^+ \rightarrow CO + HCNH^+$ $HCN + H^+ \rightarrow H + HNC^+$ $HCN + ph \rightarrow H + CN$	$HCN + C^+ \rightarrow H + CNC^+$ $HCN + ph \rightarrow H + CN$	$HCN + ph \rightarrow H + CN$ $HCN + C^+ \rightarrow H + CNC^+$
		Production	
	$N + CH_2 \rightarrow H + HCN$ $H + CCN \rightarrow C + HCN$ $HCNH^+ + e^- \rightarrow H + HCN$ $C + HNC \rightarrow C + HCN$	$H + CCN \rightarrow C + HCN$ $HCNH^+ + e^- \rightarrow H + HCN$	$HCNH^+ + e^- \rightarrow H + HCN$ $H + CCN \rightarrow C + HCN$

Enoch, M. L., Evans, Neal J., I., Sargent, A. I., & Glenn, J. 2009, ApJ, 692, 973

Enoch, M. L., Glenn, J., Evans, Neal J., I., et al. 2007, ApJ, 666, 982

Evans, Neal J., I., Allen, L. E., Blake, G. A., et al. 2003, PASP, 115, 965

Evans, Neal J., I., Dunham, M. M., Jørgensen, J. K., et al. 2009, ApJS, 181, 321

Francis, L., Johnstone, D., Dunham, M. M., Hunter, T. R., & Mairs, S. 2019, ApJ, 871, 149

Fuente, A., Martin-Pintado, J., Cernicharo, J., & Bachiller, R. 1993, A&A, 276, 473

Fuente, A., Martin-Pintado, J., & Gaume, R. 1995, ApJ, 442, L33

Goldsmith, P. F., Snell, R. L., Hemeon-Heyer, M., & Langer, W. D. 1984, ApJ, 286, 599

Green, J. D., Evans, Neal J., I., Jørgensen, J. K., et al. 2013, ApJ, 770, 123

Han, X. H., Zhou, J. J., Wang, J. Z., et al. 2015, Astronomy and Astrophysics, 576, A131

Harvey, P., Merín, B., Huard, T. L., et al. 2007, ApJ, 663, 1149

Heays, A. N., Bosman, A. D., & van Dishoeck, E. F. 2017, A&A, 602, A105

Hogerheijde, M. R., van Dishoeck, E. F., Salverda, J. M., & Blake, G. A. 1999, ApJ, 513, 350

Hull, C. L. H., Girart, J. M., Tychoniec, Ł., et al. 2017, ApJ, 847, 92

Hurt, R. L. & Barsony, M. 1996, ApJ, 460, L45

Jørgensen, J. K. 2004, A&A, 424, 589

Karska, A., Herczeg, G. J., van Dishoeck, E. F., et al. 2013, A&A, 552, A141

Karska, A., Kaufman, M. J., Kristensen, L. E., et al. 2018, ApJS, 235, 30

Karska, A., Kristensen, L. E., van Dishoeck, E. F., et al. 2014, A&A, 572, A9

Kristensen, L. E., van Dishoeck, E. F., Mottram, J. C., et al. 2017, A&A, 605, A93

Kristensen, L. E., van Dishoeck, E. F., van Kempen, T. A., et al. 2010, A&A, 516, A57

Kroupa, P. 2002, Science, 295, 82

Lada, C. J. 1987, in IAU Symposium, Vol. 115, Star Forming Regions, ed. M. Peimbert & J. Jugaku, 1

Larson, R. B. 2003, Reports on Progress in Physics, 66, 1651

Lee, K. I., Fernández-López, M., Storm, S., et al. 2014, ApJ, 797, 76

Manoj, P., Watson, D. M., Neufeld, D. A., et al. 2013, ApJ, 763, 83

McMullin, J. P., Mundy, L. G., Blake, G. A., et al. 2000, ApJ, 536, 845

Myers, P. C. & Ladd, E. F. 1993, ApJ, 413, L47

Ortiz-León, G. N., Dzib, S. A., Kounkel, M. A., et al. 2017, ApJ, 834, 143

Riaz, B., Thi, W. F., & Caselli, P. 2018, MNRAS, 481, 4662

Schöier, F. L., van der Tak, F. F. S., van Dishoeck, E. F., & Black, J. H. 2005, A&A, 432, 369

Skrutskie, M. F., Cutri, R. M., Stiening, R., et al. 2006, AJ, 131, 1163

Spaans, M., Hogerheijde, M. R., Mundy, L. G., & van Dishoeck, E. F. 1995, ApJ, 455, L167

Stäuber, P., Benz, A. O., Jørgensen, J. K., et al. 2007, A&A, 466, 977

Suresh, A., Dunham, M. M., Arce, H. G., et al. 2016, AJ, 152, 36

Testi, L. & Sargent, A. I. 1998, ApJ, 508, L91

Thi, W. F., van Zadelhoff, G. J., & van Dishoeck, E. F. 2004, Astronomy and Astrophysics, 425, 955

van der Tak, F. F. S., Black, J. H., Schöier, F. L., Jansen, D. J., & van Dishoeck, E. F. 2007, A&A, 468, 627

van Dishoeck, E. F. 1987, in IAU Symposium, Vol. 120, Astrochemistry, ed. M. S. Vardya & S. P. Tarafdar, 51–65

van Dishoeck, E. F., Kristensen, L. E., Benz, A. O., et al. 2011, PASP, 123, 138

van Kempen, T. A., van Dishoeck, E. F., Güsten, R., et al. 2009, A&A, 507, 1425

Wakelam, V., Herbst, E., Loison, J. C., et al. 2012, ApJS, 199, 21

Walker-Smith, S. L., Richer, J. S., Buckle, J. V., Hatchell, J., & Drabek-Maunder, E. 2014, MNRAS, 440, 3568

Wright, E. L., Eisenhardt, P. R. M., Mainzer, A. K., et al. 2010, AJ, 140, 1868

Yıldız, U. A., Kristensen, L. E., van Dishoeck, E. F., et al. 2015, A&A, 576, A109

Yoo, H., Lee, J.-E., Mairs, S., et al. 2017, ApJ, 849, 69

Zuckerman, B., Kuiper, T. B. H., & Rodriguez Kuiper, E. N. 1976, ApJ, 209, L137

Appendix A: Spectral Energy Distributions

Broad-band observations are needed in order to determine physical properties of a protostar. Dunham et al. 2015 studied properties of protostars in the Serpens molecular cloud using 2MASS (Skrutskie et al. 2006) and Spitzer IRAC/MIPS (Evans et al. 2009), observations covering the range of 1.25–70 μm, photometry from Wide-field Infrared Survey Explorer 12 and 22 μm (WISE; Wright et al. 2010), SHARC-II 350 μm (Suresh et al. 2016), the SCUBA Legacy Catalog 450 and 850 μm (Di Francesco et al. 2008) and 1.1 mm observations from Bolocam dust survey (Enoch et al. 2007). The Serpens Main region was also observed during the Herschel Gould Belt survey project (André et al. 2010). SPIRE/PACS photometry in the Serpens molecular cloud is discussed in Fiorellino et al. (in prep.).

Based on SEDs the bolometric temperature and luminosity can be calculated for each of the observed protostars. The bolometric luminosity was determined by integrating the SEDs over frequency:

$$L_{bol} = \pi d^2 \int F_\nu d\nu \qquad (A.1)$$

where d is the cloud distance of 436 ± 9.2 pc (Ortiz-León et al. 2017). The bolometric temperature was calculating as described in Myers & Ladd 1993:

$$T_{bol} = 1.25 \, 10^{-11} \, \bar{\nu} \qquad (A.2)$$

where $\bar{\nu}$ is the mean frequency given by:

$$\bar{\nu} = \frac{\int \nu F_\nu d\nu}{\int F_\nu d\nu} \qquad (A.3)$$

Using Scipy *splrep* and *splev* functions cubic smooth spline interpolation of the photometric data was performed while calculating the protostars parameters. Integration along the resulting axis was obtain with the composite trapezoidal rule (*Scipy* package). The photometric data allows us to perform the integration along wide range of wavelength with exception of SMM8. Here we have only 4 photometric points from the Herschel Gould Belt so the calculated bolometric luminosity and temperature can be underestimated.

Appendix B: Molecular emission maps

Appendix C: Flux correlations

Appendix D: Wings emission

Appendix E: Astrochemical models

Appendix F: Dominant reactions in CN, HCN chemistry
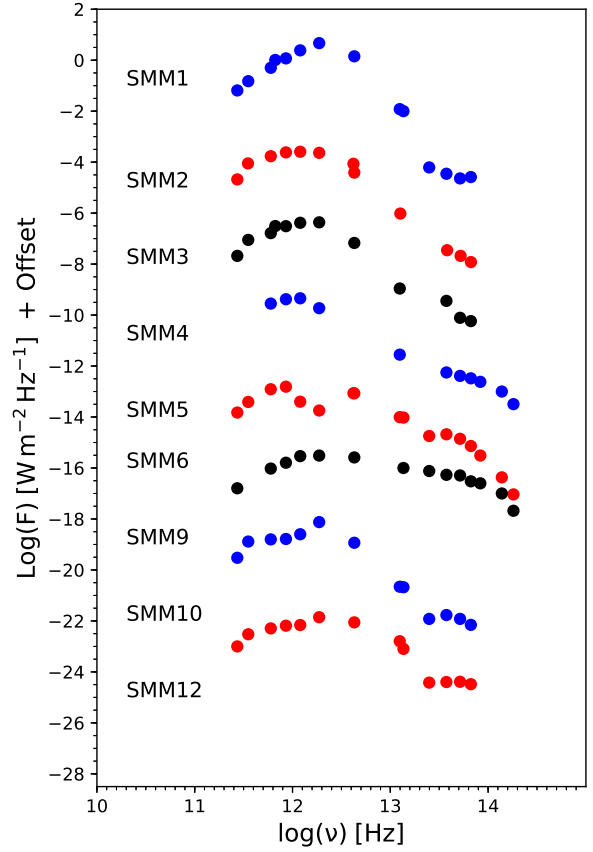
Fig. A.1: Spectral Energy Distributions of protostars in the Serpens Main region.
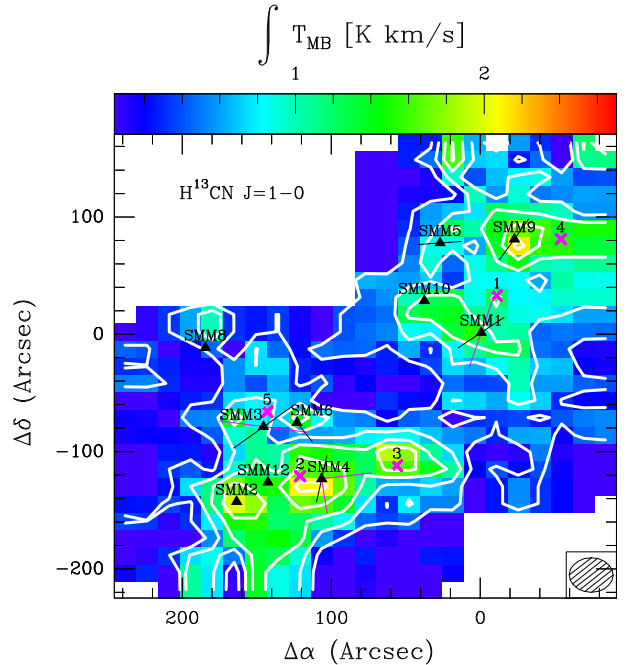
Fig. B.1: Similar to Fig. 2 but the emission of the H^{13}CN $J = 1 - 0$ line. The first contour at 10 σ level, with step of 10 σ
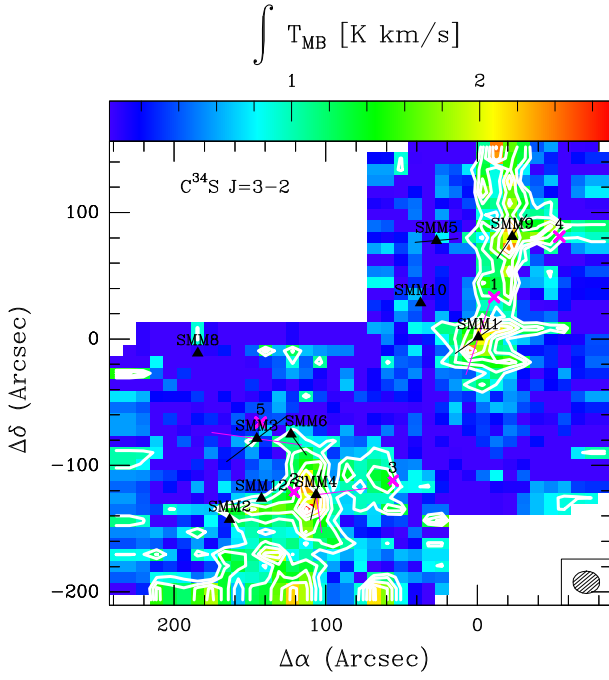
Fig. B.2: Similar to Fig. 2 but the emission of the $C^{34}S$ $J = 3 - 2$ line. The first contour at 30 σ level, with step of 10 σ
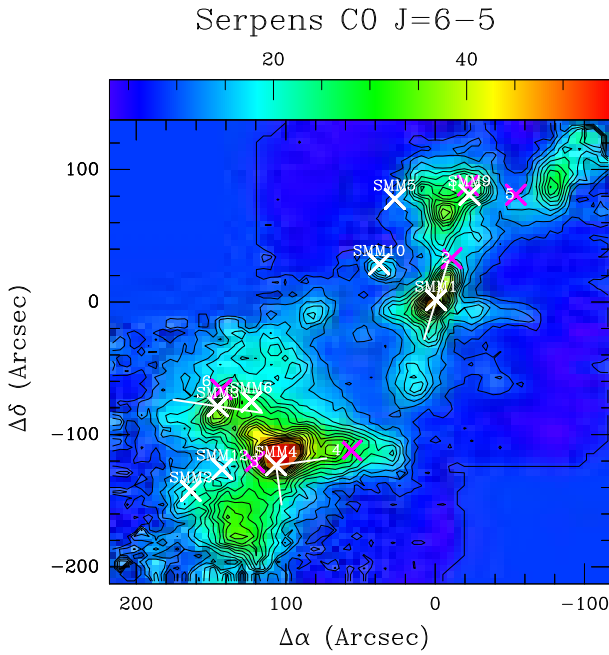
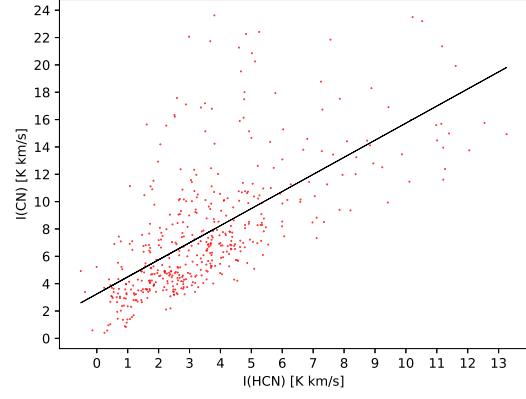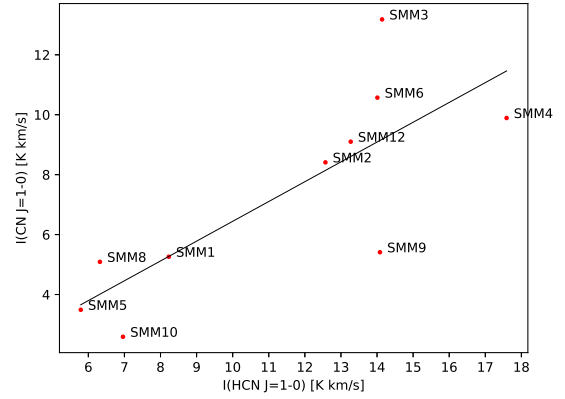Fig. B.3: APEX map: the emission of the CO $J = 6 - 5$ line.

Fig. C.1: Correlation of CN $J = 1 - 0$ and HCN $J = 1 - 0$ integrated intensities $\int T_{mb} \, dV$ for every pixel. A least-squares linear regresion (black line) with following parametes: slope = 1.25, intercept = 0.24, stderr = 0.07. The Pearson correlation coefficient equals 0.65.

Fig. C.2: Correlation of $CN J = 1 - 0$ and $HCN J = 1 - 0$ integrated intensities $\int T_{mb} \, dV$ for all sources. A least-squares linear regresion (black line) with following parametes: slope = 0.66, intercept = -0.17, stderr = 0.18. The Pearson correlation coefficient equals 0.79.
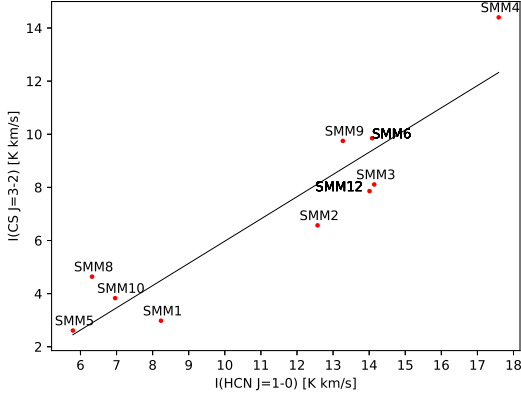
Fig. C.3: Similar to Fig. C.2 but CS $J = 3 - 2$ and HCN $J = 1 - 0$ lines correlation. A least-squares linear regresion (black line) with following parametes: slope = 0.83, intercept = -2.39, stderr = 0.12. The Pearson correlation coefficient equals 0.93.
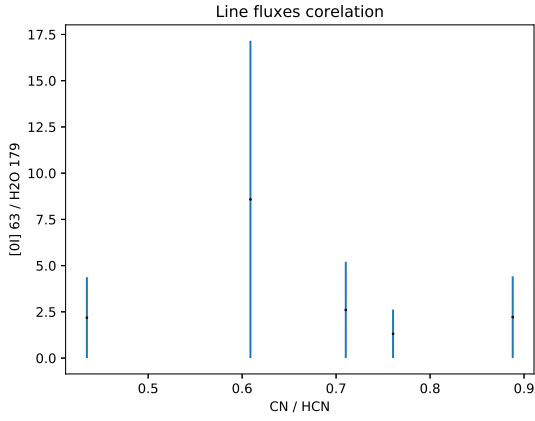
Fig. C.4: Correlation of [OI] 63 μm and H_2O 179 μm fluxes.
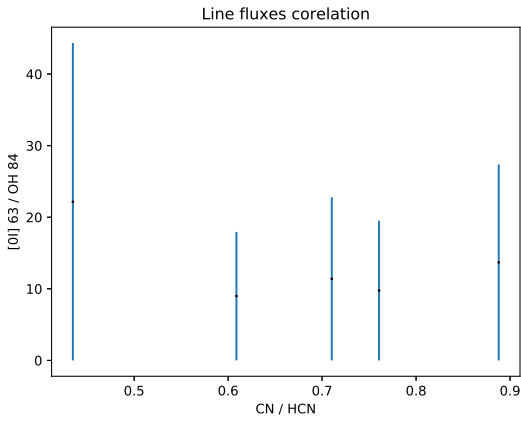
Fig. C.5: Correlation of [OI] 63 μm and OH 84 μm fluxes.
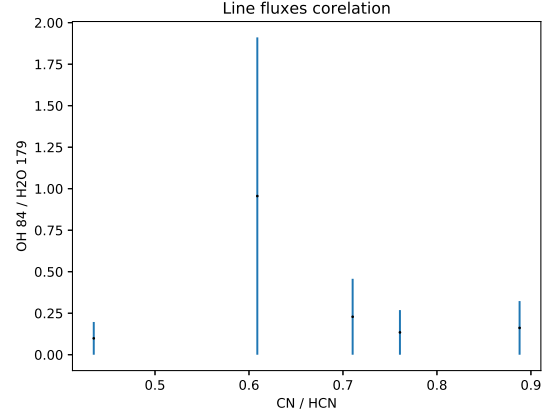
Fig. C.6: Correlation of OH 84 μm and H_2O 179 μm fluxes.
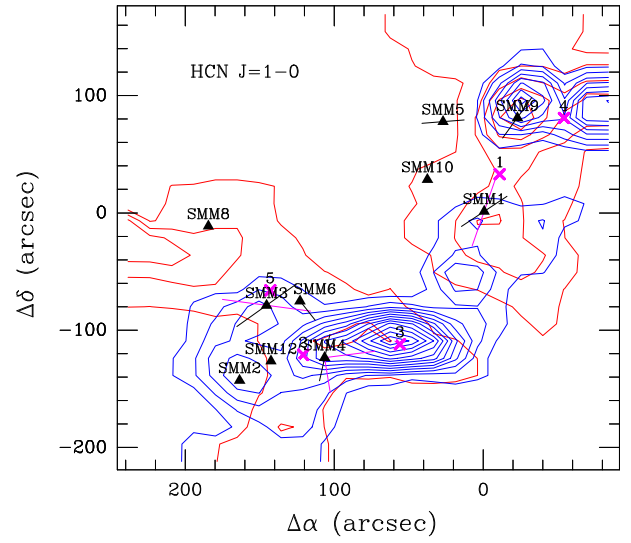
Fig. D.1: HCN $J = 1 - 0$ blue-shifted and red-shifted emission in Serpens Main region. The first contour is at 5 σ with the step of 3 σ. Triangles and lines marked as decribed in 2.
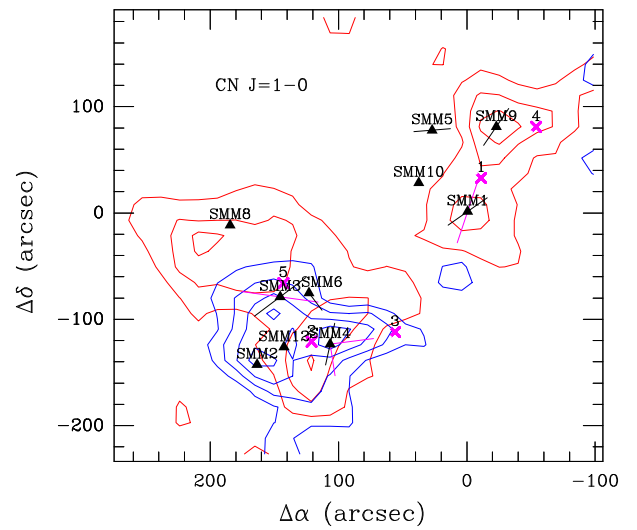
Fig. D.2: Similar to Fig. D.1 but the emission of the CN $J = 1-0$ line.
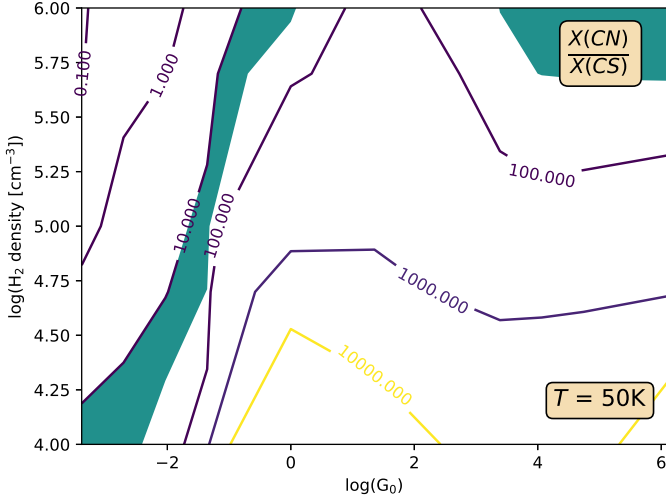
Fig. E.1: Similar to Fig. 8 but for CN/CS ratio.
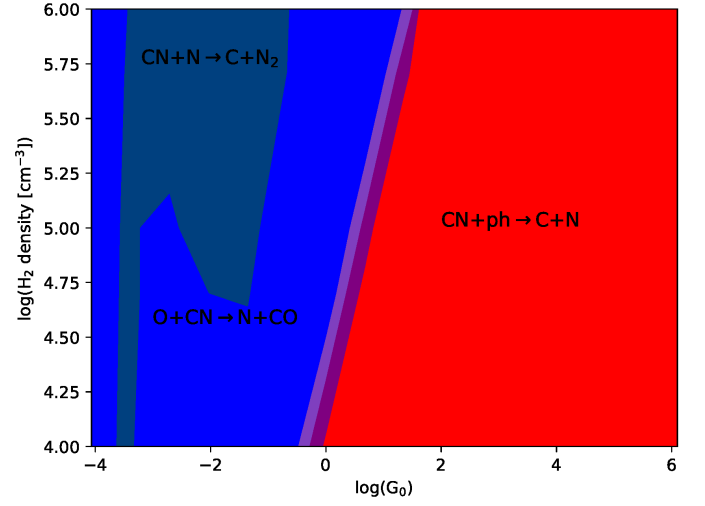
Fig. F.1: Dominant reactions of CN destruction. Reactions contributed at least 50% of total flux are marked with full colous. Transparent colours correspond to 30%-50% contribution.
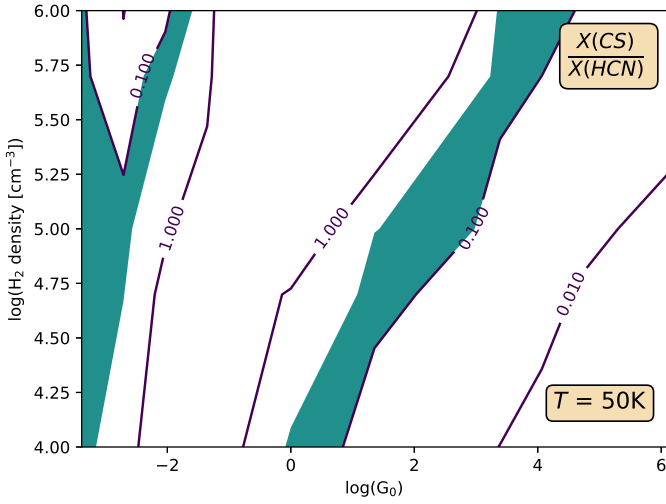
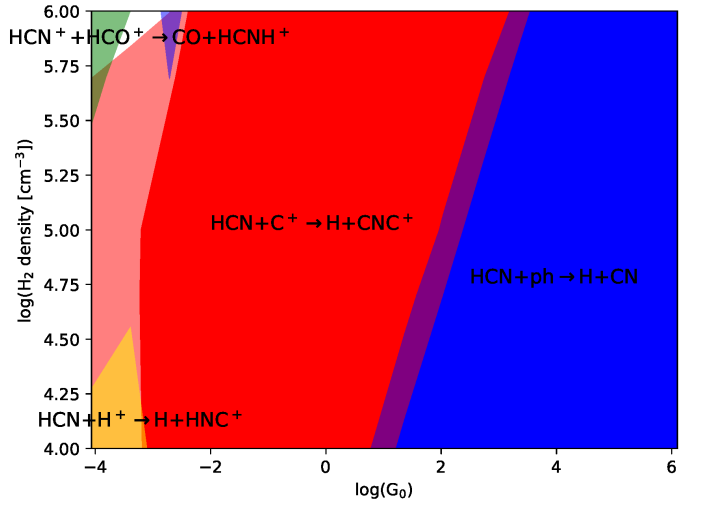

Fig. E.2: Similar to Fig. 8 but for CS/HCN ratio.

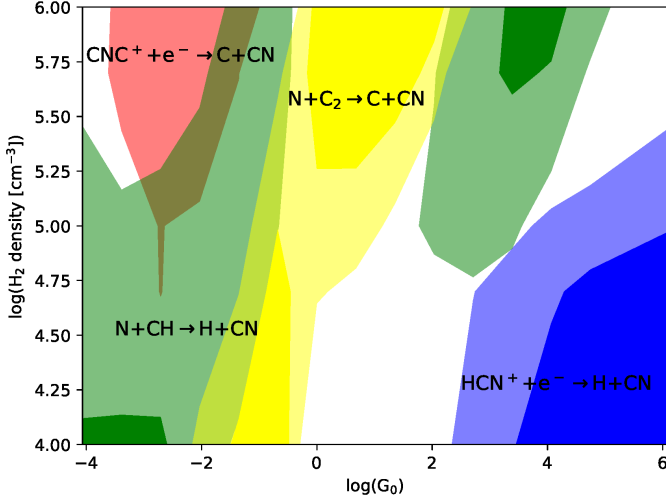Fig. F.2: Similar to Fig. F.1 but for HCN destruction.

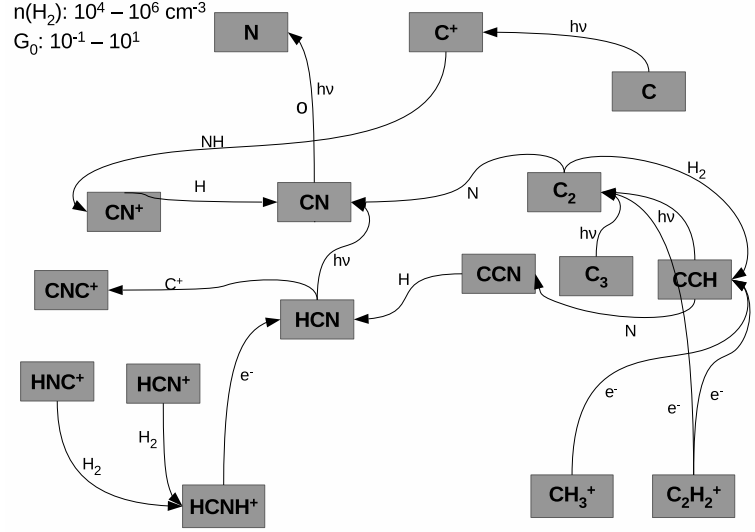Fig. F.3: Similar to Fig. F.1 but for CN production.

Fig. F.6: Similar to Fig. F.5 but for UV field of $G_0 = 10^{-1} - 10^1$).
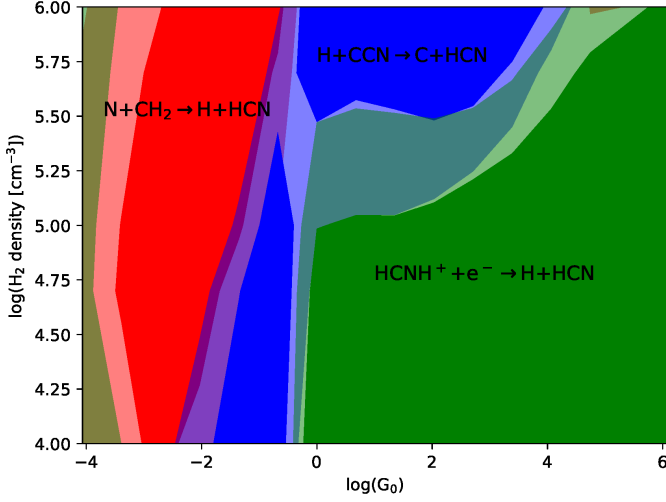

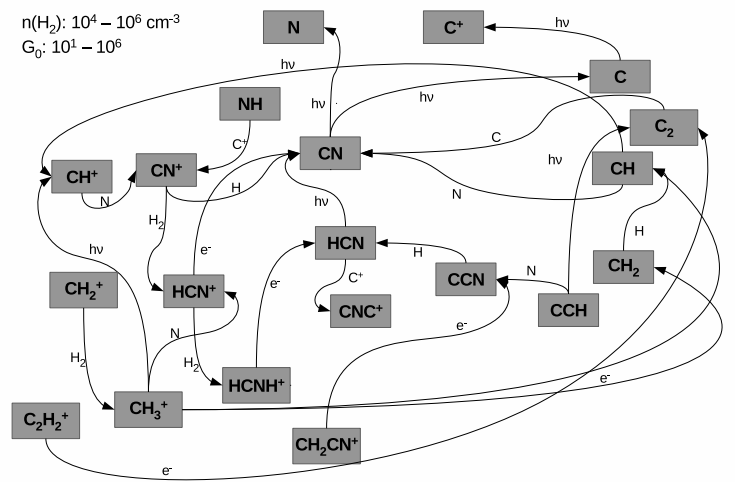Fig. F.4: Similar to Fig. F.1 but for HCN production.

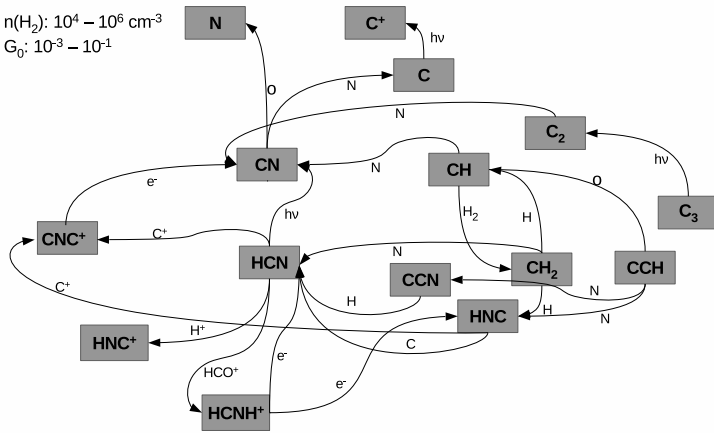Fig. F.7: Similar to Fig. F.5 but for for UV field higher than $G_0 = 10^1$).

Fig. F.5: Reactions network for weakly UV irradiated gas.